

UNIVERSIDADE FEDERAL DA GRANDE DOURADOS - UFGD

FACULDADE DE ENGENHARIA

ENGENHARIA MECÂNICA

THALES RODRIGUES PRETTO

**ANÁLISE AERODINÂMICA EXPERIMENTAL DE UMA ASA FRONTAL
MULTI-ELEMENTO TIPO FÓRMULA**

DOURADOS – MS 2025

THALES RODRIGUES PRETTO

**ANÁLISE AERODINÂMICA EXPERIMENTAL DE UMA ASA FRONTAL
MULTI-ELEMENTO TIPO FÓRMULA**

Trabalho de Conclusão de Curso apresentado ao Curso de Engenharia Mecânica da Universidade Federal da Grande Dourados, como requisito parcial para obtenção do título de Bacharel em Engenharia Mecânica.

Área de concentração: Mecânica dos Fluidos Experimental.

Orientador: Augusto Salomão Bornschlegell

DOURADOS – MS 2025



MINISTÉRIO DA EDUCAÇÃO
FUNDAÇÃO UNIVERSIDADE FEDERAL DA GRANDE DOURADOS

ANEXO D - AVALIAÇÃO FINAL DO TRABALHO DE CONCLUSÃO DE CURSO

Aluno: **THALES RODRIGUES PRETTO**

Título do trabalho e subtítulo (se houver): **Experimental Analysis of Aerodynamic Sensitivity and Interference Effects on a Formula-Style Multi-Element Front Wing.**

BANCA EXAMINADORA

1. Presidente (orientador):

Prof. Dr. Augusto Salomão Bornschlegell, Universidade Federal da Grande Dourados - UFGD

2. Membro:


Prof. Dr. Bruno Arantes Moreira, Universidade Federal da Grande Dourados - UFGD

3. Membro:


Profa. Dra. Isabele Oliveira de Paula, Universidade Federal da Grande Dourados - UFGD

De acordo com o grau final obtido pelo aluno, nós da banca examinadora, declaramos **APROVADO** o aluno acima identificado, na componente curricular Trabalho de Conclusão de Curso (TCC-II) de Graduação no Curso de Engenharia Mecânica da Universidade Federal da Grande Dourados.


Dourados, 03 de dezembro de 2025.

Documento assinado digitalmente
 **AUGUSTO SALOMAO BORNSCHLEGELL**
Data: 04/12/2025 10:06:46-0300
Verifique em <https://validar.iti.gov.br>

Prof. Dr. Augusto Salomão Bornschlegell

Documento assinado digitalmente
 **BRUNO ARANTES MOREIRA**
Data: 03/12/2025 21:58:11-0300
Verifique em <https://validar.iti.gov.br>

Prof. Dr. Bruno Arantes Moreira

Documento assinado digitalmente
 **ISABELE OLIVEIRA DE PAULA**
Data: 04/12/2025 09:37:15-0300
Verifique em <https://validar.iti.gov.br>

Profa. Dra. Isabele Oliveira de Paula

Resumo: Este trabalho investiga as forças aerodinâmicas em uma asa frontal multi-elemento inspirada na Fórmula 1, operando no regime de Baixo Número de Reynolds. Através de uma abordagem experimental utilizando um protótipo em escala produzido via manufatura aditiva e testado em túnel de vento com esteira rolante, o estudo explora a complexa interação entre efeito solo, ângulo de ataque e velocidade do escoamento. Central a esta análise está o "Efeito Cascata", um mecanismo crítico para a geração de alta sustentação, cuja eficácia é rigorosamente examinada sob condições variadas. Os resultados revelam um panorama não linear de desempenho aerodinâmico, desafiando suposições clássicas sobre a proximidade do solo e revelando a suscetibilidade de perfis de alta curvatura a fenômenos de estol abrupto quando o mecanismo de cascata falha. Por fim, esta pesquisa destaca o delicado equilíbrio necessário para maximizar a eficiência aerodinâmica (razão sustentação-arrasto), demonstrando que o melhor ponto de operação não é alcançado através da maximização de parâmetros individuais, mas através do ajuste preciso das restrições geométricas e de escoamento.

ENC-2026-XXXX

Experimental Aerodynamic Analysis of a Formula-Style Multi-Element Front Wing

Thales Rodrigues Pretto

Augusto Salomão Bornschlegell

Federal University of Grande Dourados - UFGD

thalesr883@gmail.com

augustosalomao@ufgd.edu.br

Abstract. This work investigates the aerodynamic forces on a Formula 1-inspired multi-element front wing operating within the Low Reynolds Number regime. Through an experimental approach using a scale prototype produced via additive manufacturing and tested in a wind tunnel with a rolling road, the study explores the intricate interplay between ground effect, angle of attack, and flow velocity. Central to this analysis is the "Cascade Effect," a critical mechanism for high-lift generation, whose efficacy is rigorously examined under varying conditions. The results unveil a non-linear landscape of aerodynamic performance, challenging classical assumptions regarding ground proximity and revealing the susceptibility of high-camber profiles to abrupt stall phenomena when the cascade mechanism falters. Ultimately, this research highlights the delicate equilibrium required to maximize aerodynamic efficiency (lift-drag ratio), demonstrating that best operating point is achieved not through the maximization of individual parameters, but through the precise tuning of geometric and flow constraints.

Keywords: Multi-element Wing, Ground Effect, Low Reynolds Number, Downforce, Automotive Aerodynamics.

1. INTRODUCTION

In high-performance motorsport, such as Formula 1, the central engineering challenge is maximizing tire grip, which determines the limit of cornering speed. The aerodynamic solution to this challenge is the generation of negative lift, or downforce. Joseph Katz (1995) defines downforce as the vertical aerodynamic force, deliberately directed downwards, applied to the chassis. Its purpose is to increase the normal force pressing the tires against the asphalt, raising the available grip limit and, consequently, allowing the vehicle to negotiate curves at higher speeds. However, downforce generation is intrinsically accompanied by aerodynamic drag, a resistive force that opposes motion and limits maximum straight-line speed. Therefore, aerodynamic engineering in F1 is an exercise in managing this cost/benefit balance (Suvanjumrat *et al.*, 2025).

To quantify and compare these forces universally, regardless of model size or atmospheric conditions, dimensionless coefficients are used (Anderson, 2007). The Lift Coefficient (C_L) and Drag Coefficient (C_D) normalize the measured forces (L and D , respectively) relative to the air's kinetic energy—known as dynamic pressure ($q = \frac{1}{2}\rho V^2$)—and a body reference area (S). In the context of this work, C_L represents the magnitude of downforce, and the designer's goal is to maximize this coefficient while minimizing C_D .

The study of a single airfoil, although simpler, reveals a fundamental limitation: flow separation (stall) occurs at relatively low angles of attack. Beyond this critical angle, lift (downforce) decreases, and drag increases sharply (Chiplunkar *et al.*, 2023). Specifically in high camber profiles, such as those used in this study, this phenomenon can manifest in two ways, as illustrated in Figure 1: a gradual stall, initiated at the trailing edge (trailing edge separation), or an abrupt stall, caused by sudden separation at the leading edge (leading edge separation) (Katz, 2006).

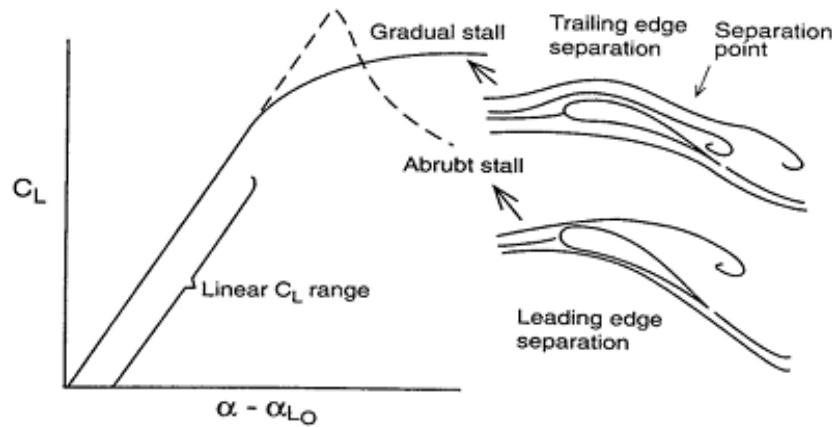


Figure 1: Effect of stall type (gradual vs. abrupt) on the C_L versus α curve, and the corresponding flow separation at the trailing edge and leading edge.

Source: Katz (2006, p. 106)

To overcome this limitation, designers evolved towards complex multi-element wing sets (Katz, 2006). The effectiveness of these systems lies in the "Cascade Effect." As described by (Katz, 2006), this phenomenon uses precisely designed slots between profiles to guide high-pressure air from the pressure side (lower surface) to the suction side (upper surface) of the subsequent element. This high-energy "blowing" re-energizes the boundary layer, delaying stall and allowing the assembly to operate at much more aggressive angles of attack.

However, this high performance is intrinsically linked to extreme sensitivity to configuration parameters. Performance is not merely the sum of components but the result of a complex flow interaction. If the relative geometry—defined by the angle of attack or ground proximity—is not optimal, the interaction can become negative, generating counter-intuitive effects. Ground proximity sensitivity (Ground Effect) is a classic example, where the literature (Zhang *et al.*, 2006; Abood and Hussain, 2024) predicts an amplification of downforce as height (h/c) decreases. Although the general trend is amplification, the behavior is not necessarily linear; Abood and Hussain (2024), for instance, observed a non-linear optimization behavior in their study, reinforcing the complexity of the interaction.

Finally, the complexity of this study is amplified by the operation in the Low Reynolds Number regime ($Re < 20,000$), which reflects the testing conditions of this document. In this regime, the flow is susceptible to the formation of "separation bubbles," illustrated in Figure 2, which alter boundary layer behavior (Katz, 2006). Furthermore, aerodynamic performance is known to be affected, with $C_{L_{max}}$ (maximum lift coefficient) typically being reduced compared to high Re regimes.

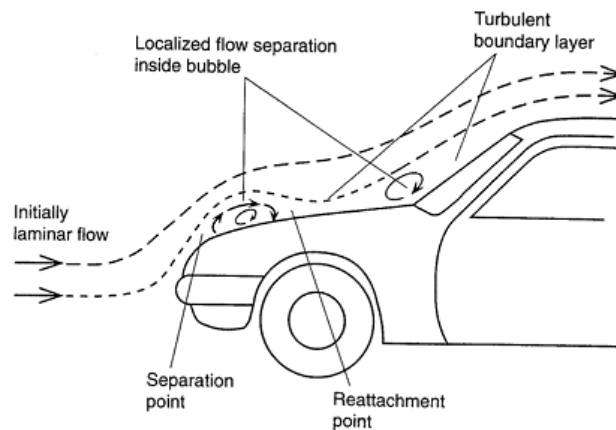


Figure 2: Schematic description of a laminar separation bubble and the laminar-to-turbulent boundary layer transition, typical of low Reynolds Number flows.

Source: Katz (2006, p. 34)

This work presents an experimental investigation of these phenomena. Using a tetra-parted model inspired by the Mercedes W11 and realized through additive manufacturing, wind tunnel tests were conducted. The objective is to characterize the wing's aerodynamic sensitivity by varying its angle of attack and ground height, to quantify not only

its peak performance but also to identify and analyze regimes of destructive interference—such as abrupt stall or reverse ground effect, in contrast to classical literature—and their implications on aerodynamic performance.

2. METHODOLOGY

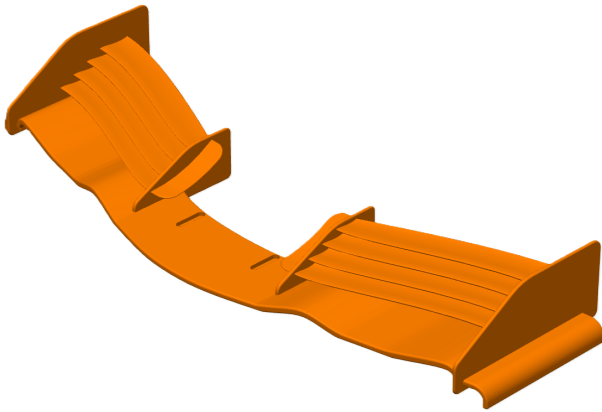
For the experimental study discussed herein, controlled tests were conducted in a wind tunnel using a self-built prototype. The experimental apparatus used, composed of the prototype model, a wind tunnel, and an instrumental support, was duly calibrated for data acquisition and filtering. With the filtered data, an analytical reduction of the raw data was chosen to characterize the aerodynamic sensitivity of the model based on the literature, enabling subsequent discussion.

2.1 Experimental Model and Additive Manufacturing

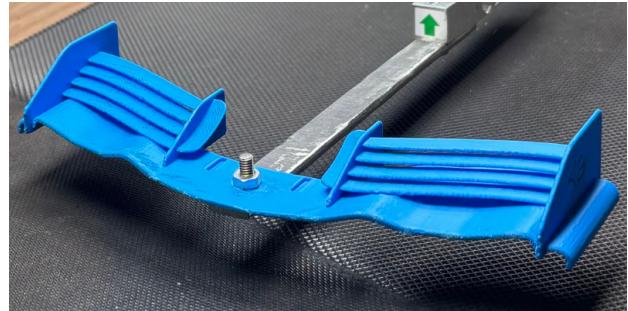
The experimental model used was inspired by the front wing of the Mercedes Formula 1 prototype, the Mercedes AMG F1 W11 EQ Performance. For its realization, the CAD development software *SolidWorks* was used to create sketches and finalize the model. The adapted model can be seen in Figure 3, and its geometry is based on the S1210 high-lift airfoil, developed by Michael Selig at the University of Illinois (UIUC) for SAE Heavy Lift competitions (Selig, 2025).

Based on the prototype layout (see Figure 3), the reference geometry was defined to include all surfaces generating aerodynamic forces. The reference area (S) was calculated by summing the planform areas of the multi-element sections (left and right), the central support profiles, and the central support plate. The reference chord (c_{ref}) was defined as the base profile chord (9.13 mm). Thus, area values were calculated based on the planform of the chord and span of all elements generating load. The reference values used in the calculations are:

- Reference Chord (c_{ref}) (Anderson, 2007): 9.13 mm
- Multi-element section span: 51.94 mm
- Length and Span of the central support plate: 21.92 x 49.31 mm
- Reference Area (S) (Anderson, 2007): $1.648 \times 10^{-2} \text{ m}^2$



(a) CAD model of the prototype.



(b) Printed prototype (additive manufacturing).

Figure 3: Isometric views of the developed tetra-parted prototype, comparing the virtual model (a) with the physical model (b).

Source: The author (2025).

Once the initial multi-element model with a base angle of attack of 2° for each profile was concretized, it was replicated for analysis by simply altering the angles of attack without major modifications; this way, the effect of the angle of attack on the prototype's aerodynamic behavior could be isolated. Figure 4 details the profile geometry for each angular configuration tested.

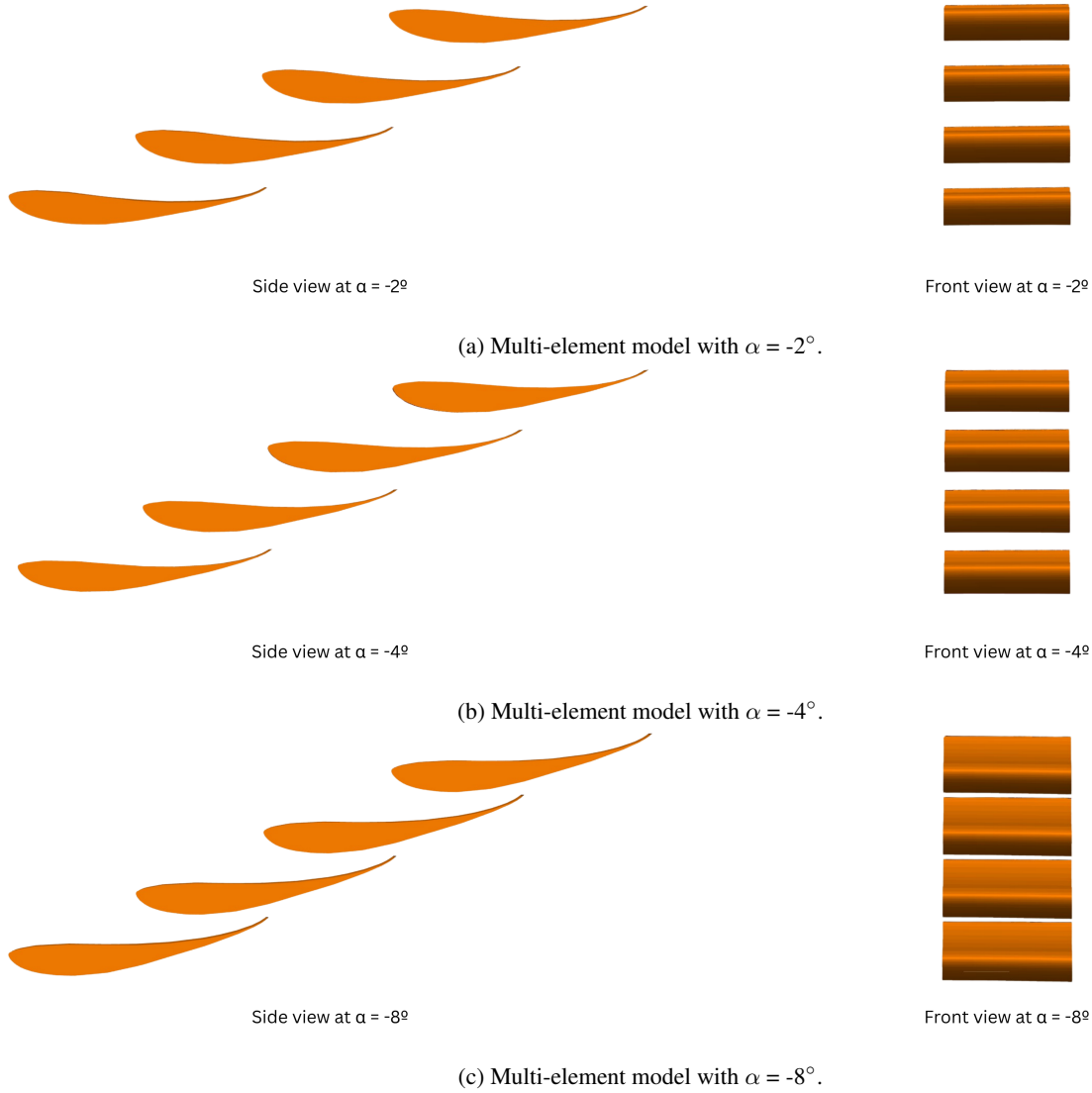


Figure 4: CAD model of the prototype detailing side and front views for each angle of attack tested.
Source: The author (2025).

With the layout of Figure 4, it is possible to visualize the "closing" of the slot occurring as the angle of attack increases from 2 to 8 degrees. This suggests that the constructive geometry of the prototype played a significant role in the results presented in this document.

For the construction of the tetra-parted test model, Fused Deposition Modeling (FDM) additive manufacturing technology was chosen. Thus, the nuances demonstrated by the profile curves and, being a scale prototype (61.65 mm x 170 mm x 23.35 mm), its smaller magnitude dimensions were compensated by the high precision obtained with high-quality 3D printing, performed by the *BambuLab* P1S printer (Bambu Lab, 2025), which has a build volume of 256 x 256 x 256 mm³, using PLA material.

2.2 Wind Tunnel

Experimental tests were conducted in the model AA-TVSH1 open-circuit horizontal wind tunnel (suction type), manufactured by Aeroalcool (Aeroalcool, 2011). This equipment features a platform measuring 1.30 m x 1.98 m x 6.2 m and a test chamber of 462 mm x 462 mm x 1200 mm.

To correctly simulate ground effect, the test section was equipped with an adapted rolling road synchronized so that its surface moved at the same velocity ($V_{\text{belt}} = V_{\text{wind}}$) as the main flow, eliminating the boundary layer relative to the ground and faithfully replicating the conditions of a moving vehicle.

2.3 Instrumentation and Acquisition System

For test execution, a specific support apparatus was built to hold the instrumentation necessary for the experiment, as well as the prototype itself, and to serve as the connection bridge between the data measurement instruments and the

electronic acquisition system. Each part of this system is described in this document, being primarily composed of:

- Adapted metallic support
- Anemometer
- Tachometer and frequency inverter (rolling road)
- Load cells
- Acquisition desk with Arduino

The adapted support (Figure 5) was constructed with two 3/8" threaded bars. The horizontal bar was fixed to a support external to the tunnel to remain isolated from vibrations exerted by the tunnel walls during operation.

A vertical bar was associated perpendicularly to the horizontal one via an adapted bushing with welded nuts. This configuration allowed the vertical bar to have its stroke (height) adjusted, being locked in the desired position by a set of nuts external to the bushing. The vertical bar featured a chamfer at the end of its stroke, where the vertically disposed load cell was bolted, as described later in this article.

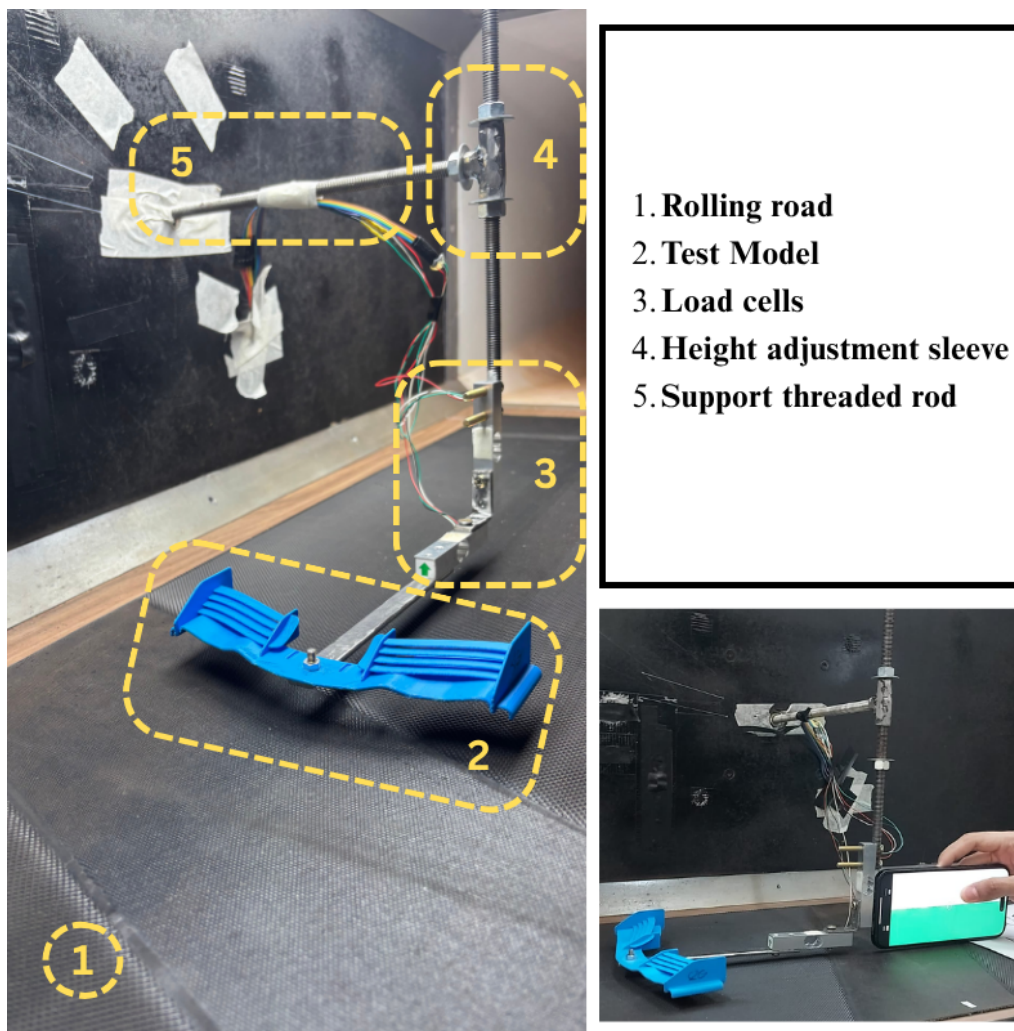


Figure 5: Adapted instrumental support for prototype positioning. The detail in the bottom corner (below the inner legend) illustrates the leveling verification procedure.

Source: The author (2025).

In association with the wind tunnel, an Extech model HD350 differential anemometer (Extech, 2025), connected to a Pitot tube, was used. The instrument was positioned in the test section to measure the actual flow velocity, allowing calibration of the relationship between wind speed and the rotation (RPM) defined in the tunnel motor's frequency inverter.

A Minipa model MDT-2238B optical (laser) tachometer (Minipa, 2025) was used to measure and calibrate the rotation speed of the rolling road. The objective was to establish the precise relationship between the motor frequency inverter and the belt's tangential velocity, ensuring correct simulation of the ground effect ($V_{\text{belt}} = V_{\text{wind}}$).

For measurement, a reflective tape was adhered to the belt surface. The tachometer's laser sensor measured the frequency of the tape passage, providing the system rotation (RPM). Based on the rotation and the belt circumference (2.1 m), the velocity (m/s) was then calculated.

To control the rotation of the adapted belt, a dedicated WEG model CFW500 inverter was used (WEG, 2025).

For aerodynamic load acquisition, two 1 kg load cells were used. One cell was oriented with its sensitivity axis in the horizontal direction (parallel to the flow) to measure Drag data. The second cell was oriented with its sensitivity axis in the vertical direction (perpendicular to the ground) to measure Lift/Downforce data.

Finally, both load cells were connected to HX711 signal amplifiers. This digitized signal was then interpreted by an Arduino Uno microcontroller. A C++ based source code was implemented on the Arduino to read the data and send it via serial communication to a computer, where it was simultaneously recorded and stored in CSV format files.

2.4 Experimental Procedure

To ensure the repeatability and precision of each of the 27 tests in the experimental matrix, the following procedure was rigorously executed for each test point:

1. **Assembly and Leveling:** The prototype was fixed to the support, and the desired height (h) was measured with a caliper by measuring the distance between the belt surface and the bottom of the wing. Next, the alignment and leveling of the apparatus were verified (as demonstrated in the lower detail of Figure 5) using the accelerometer sensor of a mobile device (Apple iPhone 15 Plus). This step was mandatory before each test to ensure that the load cells' measurement axes were perpendicular to each other and that the prototype was perfectly aligned with the flow.
2. **Tare and System Start:** The load cells were tared (zeroed) via software within the base code itself before starting each measurement. With the cells tared, the wind tunnel and rolling road were turned on using the previously noted frequency (inverter) and rotation (tachometer) values. Once the regime was reached, actual velocities were always checked and validated on the anemometer and tachometer.
3. **Data Acquisition:** The acquisition base code was then executed for a total period of 80 seconds. This time was determined to allow flow stabilization and obtain a statistically relevant sample (approximately 300 samples) for calculating the mean and standard deviation. Data were transmitted in real-time to the computer via Serial Monitor (part of the IDE) or a Python script.
4. **Finalization and Repetition:** After 80 seconds, code execution was terminated in the interface (Arduino IDE), and both the wind tunnel and belt were turned off. The apparatus was then reconfigured (new height or velocity), and the entire procedure, including the alignment check, was repeated for the next test point.

2.5 Load Sensor Calibration

To ensure precise data acquisition and convert the raw sensor signal into engineering units (gram-force, g.f), an individual calibration procedure was performed for each load cell (Lift and Drag).

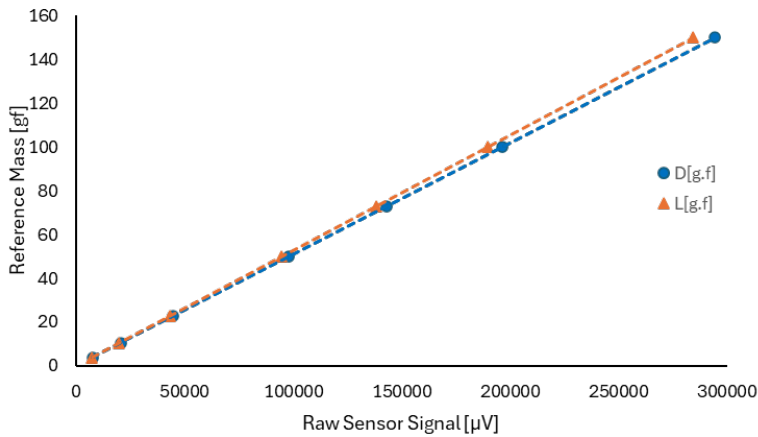
The process consisted of fixing each cell to a bench (Figure 6b), simulating its loading direction in the experiment. Reference masses, varying from 10 g to 150 g non-linearly and previously measured on a precision scale, were then applied to the load cell.

Each reference mass was applied to the cell, which was connected to the acquisition system (Arduino and HX711). The stabilized output signal (recorded in the CSV file) was associated with the corresponding mass value (g.f).

With the data pairs (Raw Signal vs. g.f), a linear regression was performed to obtain the normalization function for each sensor. The obtained functions, which convert the raw signal (x) into gram-force (y), as well as their respective coefficients of determination (R^2), were:

- **Lift Cell:** $y = 0.0005275 \cdot x + 0.0758671$; with $R^2 = 0.99999985$
- **Drag Cell:** $y = 0.0005096 \cdot x + 0.0288322$; with $R^2 = 0.99999989$

The extremely high R^2 value, close to 1, validates the sensors' perfect linearity and the calibration system's precision, as illustrated in the regression curves of Figure 6a.



(a) Linear regression curves.



(b) Bench setup.

Figure 6: Sensor calibration process: (a) resulting linear regression curves (Lift in orange/triangles; Drag in blue/circles) and (b) experimental cell setup.

Source: The author (2025).

2.6 Test Matrix

The complete test matrix was defined by combining three input parameters, which will form the basis for the results analysis: Flow Velocity, for Reynolds Number analysis (Case A), with $V = 5, 10, \text{ and } 15 \text{ m/s}$; Ground Height (Case B), with $h = 10, 15, \text{ and } 20 \text{ mm}$; and Angle of Attack (Case C), with values of $\alpha = 2^\circ, 4^\circ, \text{ and } 8^\circ$. This permutation ($3 \times 3 \times 3$) resulted in a total of 27 experimental tests. In each test, the experimental procedure was rigorously followed, and the ambient temperature was measured for the precise calculation of density (ρ). The obtained data were reserved in tables in the *Excel* software to optimize future data reduction.

3. Results and Discussion

In this section, the filtered and processed data by the methodology are presented. The analysis is structured to first validate the collected data and then isolate and investigate the influence of each of the three input parameters defined in the methodology, comparing experimental results with the literature concepts presented in the Introduction. Finally, the overall performance is synthesized through the prototype's aerodynamic efficiency.

3.1 Preliminary Data Analysis

Before analyzing performance parameters, it is fundamental to verify the quality of the collected data. Figure 7 presents a sample of the raw data time series (in g.f) for a typical test, highlighting measurement noise and flow stabilization time.

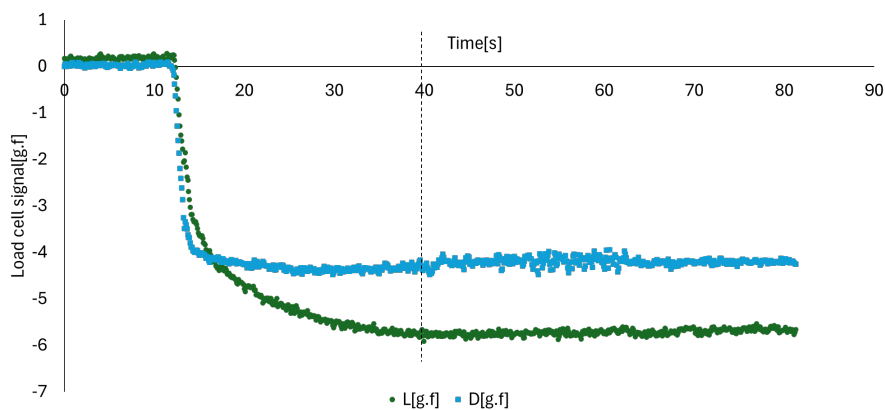


Figure 7: Time series of raw data (in g.f) from Lift and Drag load cells for a representative test. The vertical dotted line indicates the point from which data were considered in steady state.

Source: The author (2025).

As observed in Figure 7, the flow took approximately 40 seconds to reach steady state. Considering that each test had a total acquisition duration of 80 seconds, it was decided to consider only the values collected after these initial 40 seconds as valid data for loading analysis. This approach ensures that the analysis is based on a completely stabilized flow regime. The fluctuation (noise) around the mean value in these data, in turn, justifies the use of standard deviation in the methodology to quantify the statistical uncertainty of the measurements.

3.2 Case A: Influence of Reynolds Number

The first aerodynamic parameter analyzed (Case A) was the influence of velocity (and, consequently, the Reynolds Number) on the coefficients. Classical literature (e.g., (Anderson, 2007)) establishes that for high Re flows ($> 500,000$), coefficients become independent of velocity.

However, as the prototype operates at very low Reynolds ($Re < 20,000$), where phenomena such as separation bubbles are common (see Introduction, Figure 2), complex behavior was expected. Figure 8 presents the complete maps of C_L and C_D coefficients as a function of Reynolds Number for all 9 geometry configurations (combinations of height and angle of attack).

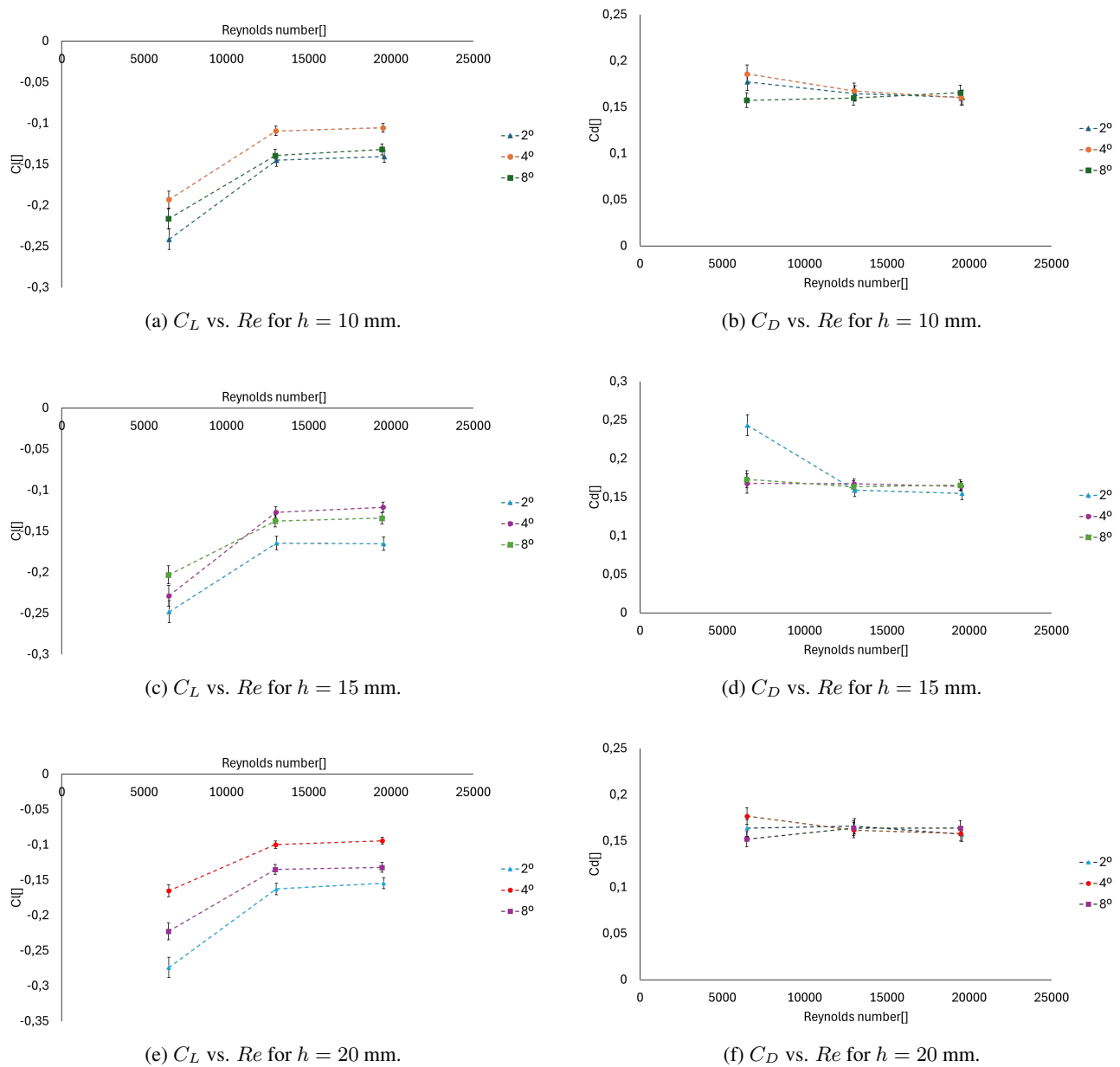


Figure 8: Maps of Lift (C_L) and Drag (C_D) Coefficients as a function of Reynolds Number (Case A) for all heights (h) and angles of attack (α) tested.

Source: The author (2025).

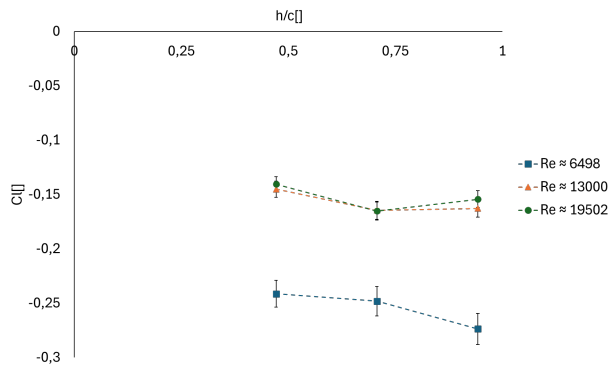
The analysis of the coefficient maps (Figure 8) reveals two distinct trends. For the Drag Coefficient (C_D), presented in the graphs on the right (b, d, f), a remarkably stable behavior is noted. Despite variations in ground height, angle of attack, and velocity, C_D remained close to the threshold of 0.15 in almost all instances.

The Downforce Coefficient (C_L), presented in the graphs on the left (a, c, e), showed a much stronger dependence on the parameters. In all 9 tested geometric configurations, there is a clear trend of decreasing downforce (the C_L value becomes less negative) as the Reynolds Number increases. This behavior, although with different magnitudes, is similar for all heights, confirming that the increase in velocity (Re) is detrimental to the prototype's performance. This trend diverges from the behavior observed by Chiplunkar *et al.* (2023), who noted a slight increase in downforce with increasing velocity in their multi-element wing.

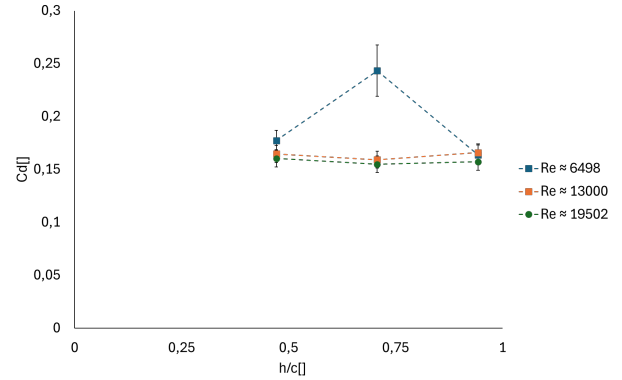
The analysis of angles of attack (the different lines in each graph) reinforces the findings that will be detailed in Case C: $\alpha = 2^\circ$ (blue line) consistently generates the highest downforce, with the peak of -0.2736 occurring at $h = 20$ mm (Figure 8e). Notably, $\alpha = 8^\circ$ (orange) generates more downforce than $\alpha = 4^\circ$ (gray), confirming the performance "valley" at $\alpha = 4^\circ$, which may indicate the proximity of a critical failure or optimization angle.

3.3 Case B: Ground Effect Analysis (Height Variation)

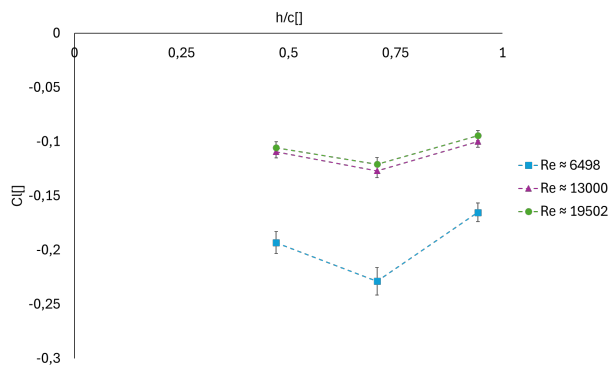
The Ground Effect (Case B) was then investigated. As discussed in the Introduction, fundamental literature (Katz, 2006; Zhang *et al.*, 2006; Abood and Hussain, 2024) predicts a complex and non-linear behavior, where ground proximity (low h/c) tends to amplify downforce but may present optimal points. The detailed experimental results, presented in Figure 9, replace the preliminary analysis and reveal this optimization behavior.



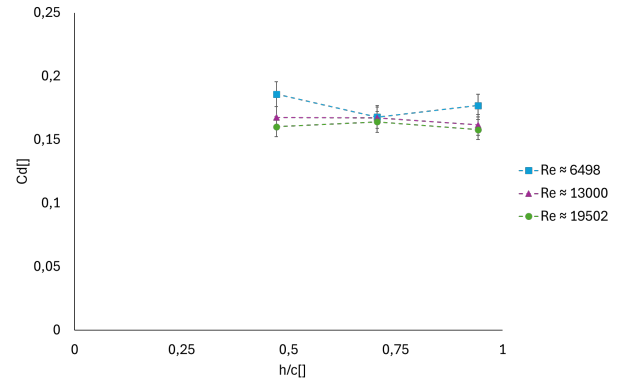
(a) C_L vs. h/c for $\alpha = 2^\circ$.



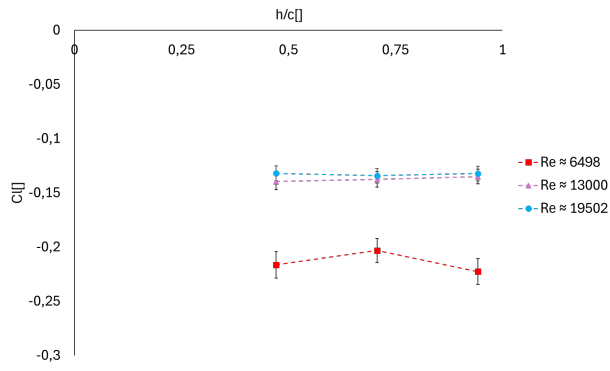
(b) C_D vs. h/c for $\alpha = 2^\circ$.



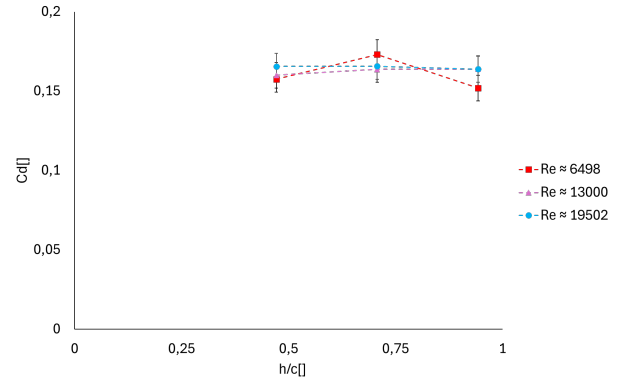
(c) C_L vs. h/c for $\alpha = 4^\circ$.



(d) C_D vs. h/c for $\alpha = 4^\circ$.



(e) C_L vs. h/c for $\alpha = 8^\circ$.



(f) C_D vs. h/c for $\alpha = 8^\circ$.

Figure 9: Maps of Coefficients (C_L and C_D) as a function of height ratio h/c (Case B) for the three angles of attack and Reynolds regimes (labeled) tested.

Source: The author (2025).

The Drag Coefficient (C_D) analysis, in the graphs on the right (Figures 9b, 9d, 9f), confirms the hypothesis from the previous section: drag is insensitive to ground height variation. The trace tends to remain stable, varying between 0.15 and 0.2 for almost all configurations. A punctual exception is observed in Figure 9b (for $\alpha = 2^\circ$), where the lowest Reynolds ($Re \approx 6,500$) presents a jump to $C_D \approx 0.25$ at $h/c = 0.71$, a phenomenon that coincides with an increase in the error bar amplitude for that point.

The Downforce Coefficient (C_L), in the graphs on the left (Figures 9a, 9c, 9e), reveals non-linear behavior, similar to that observed by Abood and Hussain (2024). For most angles and velocities, downforce (negative C_L value) increases (becomes more negative) as the wing descends from $h/c = 0.94$ to $h/c = 0.71$. However, upon reducing the height further to $h/c = 0.47$, the prototype loses performance and downforce decreases. This indicates that the height-to-chord ratio at the level of 0.71 represents the best operating point for ground effect in this geometry.

The graphs also reinforce the Case A conclusion: the highest downforce is consistently generated at the lowest Reynolds Numbers (blue lines), regardless of height or angle of attack.

3.4 Case C: The Angle of Attack Phenomenon

The analysis of the study (Case C) was the influence of the angle of attack (α). The S1210 profile is known for its high camber, which makes it susceptible to abrupt stall (leading edge separation), as illustrated in the Introduction (Figure 1).

The multi-element geometry of the prototype aims to combat this tendency through the "Cascade Effect" (Katz, 2006, p. 232). However, the experimental results (presented in Figure 10) indicate a clear limit for this mechanism.

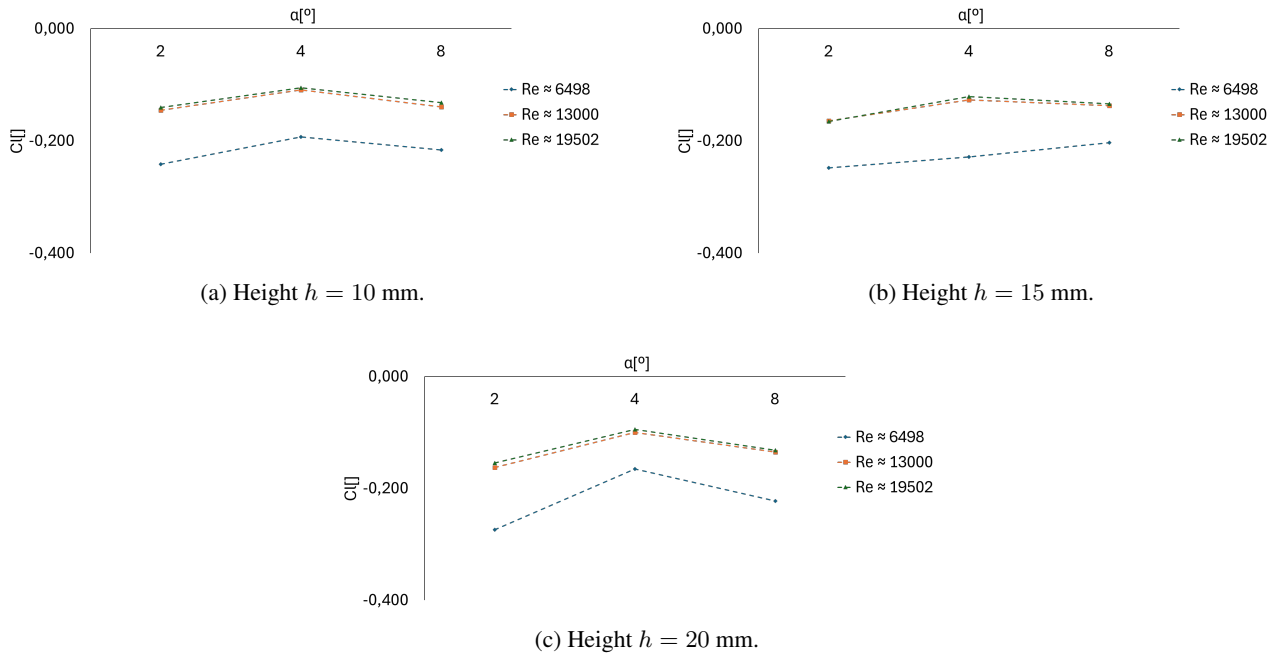


Figure 10: Lift coefficient (C_L) as a function of angle of attack (Case C) for the three ground heights, maintaining constant velocity at $V = 15$ m/s. Graphs (a), (b), and (c) highlight the performance failure at $\alpha = 4^\circ$.

Source: The author (2025).

As observed in the graphs of Figure 10, the prototype generated significant downforce at $\alpha = 2^\circ$. However, when increasing the angle to $\alpha = 4^\circ$, an abrupt drop in performance was observed at all heights. The error bars (σ_{CL}), small compared to the magnitude of the drop, confirm that this "valley" is not a measurement uncertainty but a real aerodynamic phenomenon.

The force data, therefore, *suggest* that the prototype suffered a failure of the "Cascade Effect" (Katz, 2006, p. 232). Without slot re-energization, the boundary layer (operating at Low Re) could not withstand the curvature and separated. Operation at low Reynolds numbers is notoriously challenging, as lower Re values tend to decrease $C_{L_{max}}$ and anticipate the stall angle.

The nature of the downforce loss, visible in the results of Figure 10, is consistent with the hypothesis of an "abrupt stall" (leading edge separation), illustrated earlier in Figure 1 and described by (Katz, 2006). Upon increasing to $\alpha = 8^\circ$, the system appears to be in full stall.

3.5 Performance Maps and Aerodynamic Efficiency (L/D)

Finally, to synthesize the prototype's overall performance, Aerodynamic Efficiency, defined as $E = |C_L/C_D|$, was analyzed. This index measures the ratio between generated downforce (benefit) and induced drag (cost).

Figure 11 presents a complete map of the prototype's efficiency, combining the influence of all study cases: Reynolds Number (Case A), Ground Height (Case B), and Angle of Attack (Case C).

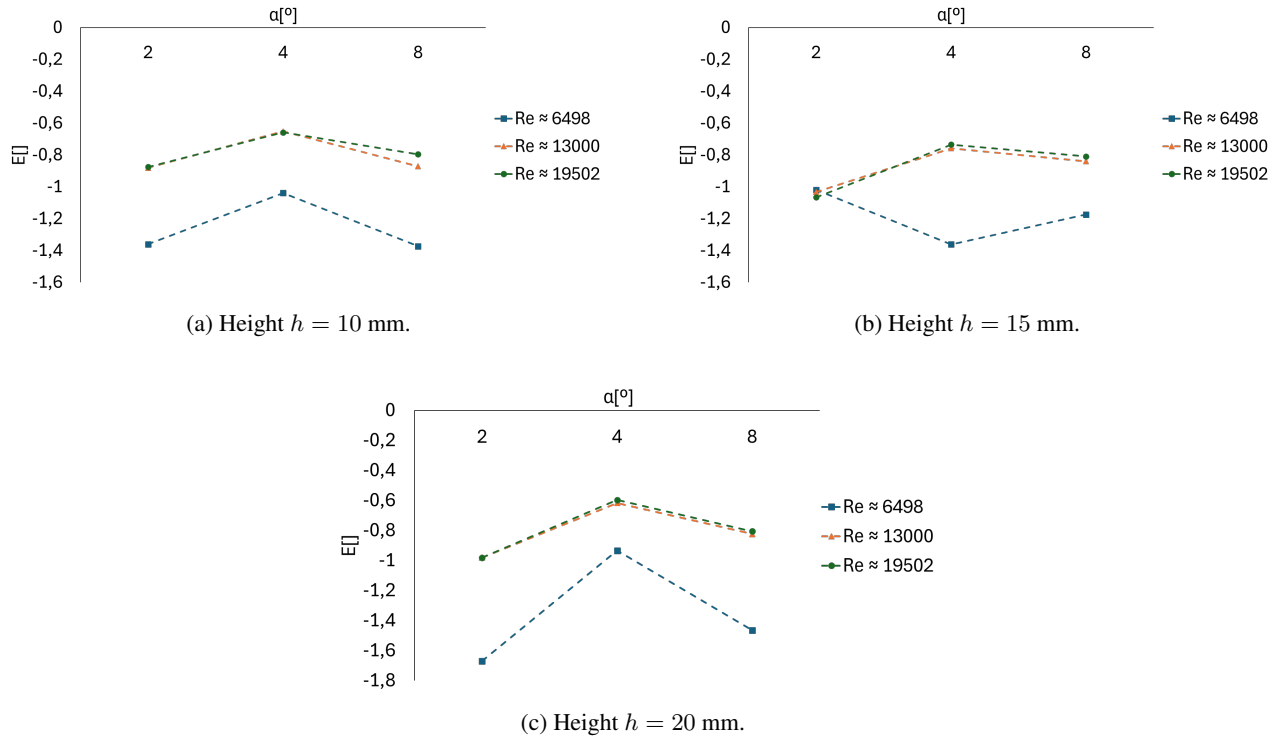


Figure 11: Aerodynamic Efficiency Map ($E = |L/D|$) as a function of angle of attack (α) and Reynolds Number (labeled lines), for the three ground heights (h) tested.

Source: The author (2025).

The efficiency map analysis (Figure 11) reinforces the conclusions of the previous sections. The performance failure at $\alpha = 4^\circ$ is a universal phenomenon for this prototype, presenting the worst efficiency at (almost) all heights and Reynolds regimes tested, with the sole exception of the 15 mm height.

Figure 11 also allows identifying the optimal operating point. It is evident that the configuration of $\alpha = 2^\circ$ for the greatest ground height ($h = 20$ mm, Figure 11c) consistently delivers the highest aerodynamic efficiency.

Within this graph (Figure 11c), it is noted that the highest efficiency (most negative E value) is reached at $\alpha = 2^\circ$. In this condition, it is the lowest Reynolds Number tested ($Re \approx 6,500$) that provides the best balance between downforce and drag, solidifying this as the prototype's highest overall performance configuration.

4. CONCLUSIONS

This work presented an experimental investigation of the aerodynamic sensitivity of a multi-element front wing, inspired by Formula 1, operating in a low Reynolds Number regime ($Re < 20,000$). The methodology, based on 27 wind tunnel tests varying velocity, ground height, and angle of attack, successfully characterized the prototype's performance and identified its critical operating points.

The results confirmed the complexity of the flow in low Reynolds, demonstrating that, unlike classical high Re theory, the prototype's aerodynamic coefficients (Case A) are dependent on velocity, with generated downforce (C_L) being inversely proportional to the Reynolds Number.

Regarding the ground effect (Case B), the analysis revealed a non-linear behavior. Contrary to the simple amplification predicted by classical theory for decreasing height, the maximum downforce was identified at an intermediate height ($h = 15$ mm), indicating an best operating point for this specific geometry.

The variation of the angle of attack (Case C), revealed a performance failure at $\alpha = 4^\circ$. In this condition, the "Cascade Effect" failed to sustain the flow. The abrupt loss of downforce is consistent with the hypothesis of an abrupt stall (leading edge separation), a common phenomenon in high-camber profiles (such as the S1210) operating in low Re .

Finally, the aerodynamic efficiency maps ($E = |L/D|$) synthesized the global performance. The configuration yielding the highest efficiency in the configuration of $\alpha = 2^\circ$, at the greatest ground height tested ($h = 20$ mm) and the lowest Reynolds Number ($Re \approx 6,500$), a condition that delivered the best balance between downforce generation and drag penalty.

5. RECOMMENDATIONS

Based on the obtained results, the following future works are suggested:

- The use of Computational Fluid Dynamics (CFD) simulations is recommended to optimize the slot geometry and ensure the effectiveness of the "Cascade Effect." Flow visualization in CFD would allow validating the design and airfoil interaction prior to additive manufacturing.
- A more detailed experimental investigation of stall points is suggested, with smaller angle of attack increments (e.g., from $\alpha = 2^\circ$ to $\alpha = 6^\circ$ in 0.5° steps). According to the literature (Katz, 2006), precise characterization of the stall type and the exact angle at which it occurs is fundamental for $C_{L_{max}}$ optimization.

6. REFERENCES

- Abood, M.S. and Hussain, I., 2024. "Ground effect of an inverted double element wing diffuser on a sedan car". *Heliyon*, Vol. 10, No. 8, p. e29435. ISSN 24058440. doi:10.1016/j.heliyon.2024.e29435. URL <https://linkinghub.elsevier.com/retrieve/pii/S2405844024054665>.
- Aeroalcool, 2011. "AA-TVSH1: Túnel de Vento Subsônico". URL <http://aeroalcool.com.br/index.php/tuneis-de-vento/25-gallery/tuneis-de-vento/29-aa-tvsh1>.
- Anderson, J.D., 2007. *Fundamentals of Aerodynamics*. McGraw-Hill Higher Education, Boston, Mass. ISBN 978-0-07-125408-3.
- Bambu Lab, 2025. "Bambu Lab P1 Series". URL <https://bambulab.com/pt-br/p1>.
- Chiplunkar, V., Gujar, R., Adiverekar, A., Kulkarni, R. and Thonge, A., 2023. "Computational fluid dynamics analysis for an active rear-wing design to improve cornering speed for a high-performance car". *Materials Today: Proceedings*, Vol. 77, pp. 887–896. ISSN 22147853. doi:10.1016/j.matpr.2022.12.040. URL <https://linkinghub.elsevier.com/retrieve/pii/S2214785322074119>.
- Extech, 2025. "Anemômetro do Tubo Pitot e Manômetro Diferencial Extech HD350". URL <https://www.mreferramentas.com.br/seguranca-e-meio-ambiente/medidores-de-fluxo-de-ar/anemometros/anemometro-do-tubo-pitot-e-manometro-diferencial-extech-hd350>.
- Katz, J., 2006. *Race car aerodynamics: designing for speed*. R. Bentley, Cambridge, Mass, revised 2nd edition edition. ISBN 978-0-8376-0142-7.
- Minipa, 2025. "MDT-2238B-1302-BR". URL https://www.minipa.com.br/images/proposta_tecnica/MDT-2238B-1302-BR.pdf.
- Selig, M.S., 2025. "S1210 12% Airfoil Data and Details". URL <http://airfoiltools.com/airfoil/details?airfoil=s1210-il>.
- Suvanjumrat, C., Namchanthra, S., Phengpom, T., Priyadumkol, J., Chookaew, W., Watechagit, S., Cheung, S.C. and Promtong, M., 2025. "AI-assisted CFD optimisation of multi-element wing angle of attack for enhanced formula SAE aerodynamic performance". *International Journal of Thermofluids*, Vol. 30, p. 101440. ISSN 26662027. doi: 10.1016/j.ijft.2025.101440. URL <https://linkinghub.elsevier.com/retrieve/pii/S2666202725003866>.
- WEG, 2025. "Inversor de Frequência CFW500". URL https://www.weg.net/catalog/weg/BR/pt/Automa%C3%A7%C3%A3o-e-Controle-Industrial/Drives/Inversores-de-Frequ%C3%Aancia/Drives-para-OEMs-e-Uso-Geral/Inversor-de-Frequ%C3%Aancia-CFW500/Inversor-de-Frequ%C3%Aancia-CFW500/p/MKT_WDC_BRAZIL_PRODUCT_INVERTER_CFW500.
- Zhang, X., Toet, W. and Zerihan, J., 2006. "Ground Effect Aerodynamics of Race Cars". *Applied Mechanics Reviews*, Vol. 59, No. 1, pp. 33–49. ISSN 0003-6900, 2379-0407. doi:10.1115/1.2110263. URL <https://asmedigitalcollection.asme.org/appliedmechanicsreviews/article/59/1/33/450607/Ground-Effect-Aerodynamics-of-Race-Cars>.